Low-Frequency Tilt Seismology with a Precision Ground-Rotation Sensor

by M. P. Ross, K. Venkateswara, C. A. Hagedorn, J. H. Gundlach, J. S. Kissel, J. Warner, H. Radkins, T. J. Shaffer, M. W. Coughlin, and P. Bodin

ABSTRACT

We describe measurements of the rotational component of teleseismic surface waves using an inertial high-precision ground-rotation sensor installed at the Laser Interferometer Gravitational-Wave Observatory (LIGO) Hanford Observatory (LHO). The sensor has a noise floor of 0.4 nrad/$\sqrt{\text{Hz}}$ at 50 mHz and a translational coupling of less than 1 μrad/m enabling translation-free measurement of small rotations. We present observations of the rotational motion from Rayleigh waves of six teleseismic events from varied locations and with magnitudes ranging from **M** 6.7 to 7.9. These events were used to estimate phase dispersion curves that show agreement with a similar analysis done with an array of three STS-2 seismometers also located at LHO.

INTRODUCTION

Measurements of the rotational components of seismic motion have gained increasing attention due to their usefulness in seismology (Lee *et al.*, 2009) along with their applications in the seismic isolation systems of ground-based gravitational-wave detectors (Lantz *et al.*, 2009). One geophysical application of these measurements is the ability to fully characterize surface waves, specifically their phase velocities, using devices placed at a single station, in contrast to the current practice of utilizing arrays of translational seismometers. These point-like measurements can lead to useful local seismological information that may be impractical to obtain using arrays while also simplifying measurement schemes (Maranó and Fäh, 2014). Rotational measurements also promise to improve seismic source inversion problems (Reinwald *et al.*, 2016). Additionally, rotation sensors of sufficient sensitivity can be used to reduce the tilt noise in horizontal seismometers (Venkateswara *et al.*, 2017), leading to improved active seismic isolation in gravitational-wave detectors.

The rotational components are henceforth referred to as the two tilts about two orthogonal horizontal axes and a torsion about a vertical axis. The tilt component along the radial direction of a teleseismic wave at a distant site can be estimated as $\kappa A = 2\pi A/\lambda$, in which A is the amplitude of the vertical displacement, κ is the seismic wavenumber, and λ is the seismic wavelength (Lee *et al.*, 2009). For amplitudes of 30 μm and wavelengths of ~70 km (typical for **M** 7 earthquake halfway around the world, measured at Hanford, Washington), this corresponds to a tilt amplitude of 3 nrad, making this measurement very challenging. Measurements of the rotational component of teleseismic events have been recorded previously for large earthquakes using sensitive ring-laser gyroscopes (Pancha *et al.*, 2000; Belfi *et al.*, 2012) in the torsional direction (about the vertical axis) or in the near-field regions using strong-motion sensors (Lin *et al.*, 2011). These measurements have had low signal-to-noise ratios (SNRs) or require strong local events to observe the rotational signals. Low coupling of the rotational output to other degrees of motion, particularly horizontal motion, is critical for teleseismic measurements as horizontal motion can mimic rotational signals if the coupling is sufficient, leading to incorrect wave parameter estimates. In the above example of teleseismic waves, a displacement cross coupling much better than κ (~10^{-4} rad/m) is required to accurately measure the tilt component.

We present the observations of the rotational component about a horizontal axis of teleseismic events with magnitudes ranging from **M** 6.7 to 7.9 originating from different parts of the world. The rotation sensor is described in detail in Venkateswara *et al.* (2014). The measurements have high SNR and have negligibly small coupling from horizontal motion. In the Instrumentation section, we describe the sensors used and their location. Subsequently, we present the framework used to characterize the surface waves. We then discuss rotational and translational data recorded from the examined earthquakes, focusing on an **M** 7.9 in Papua New Guinea. The data from the rotation sensor and an array of STS-2 seismometers at the Laser Interferometer Gravitational-Wave Observatory (LIGO) Hanford Observatory (LHO) are then analyzed to infer the angle of arrival and the Rayleigh-wave phase velocity at the site with high precision.

INSTRUMENTATION

A set of three seismometers and two ground-rotation sensors are operated as part of the advanced LIGO seismic isolation system at the LHO (Aasi *et al.*, 2015; Matichard *et al.*, 2015). The observatory is chiefly composed of three buildings: a central building (called the corner station) and two end station buildings located 4 km away. It forms a large L-shape with one

doi: 10.1785/0220170148

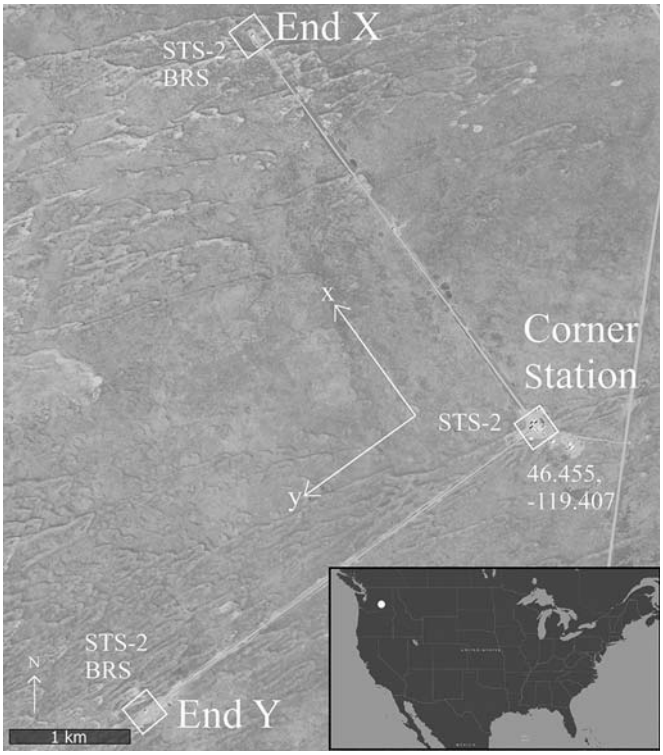

▲ **Figure 1.** Satellite image of Laser Interferometer Gravitational-Wave Observatory (LIGO) Hanford Observatory (LHO) showing the two arms: X-arm running in the northwest direction and Y-arm running in the southwest direction. Satellite image courtesy of U.S. Geological Survey (USGS). The inset shows a map of the continental United States (courtesy of USGS) and the location of the LHO.

arm (EndX) running in the northwest direction and the other (EndY) orthogonally oriented along the southwest direction as shown in Figure 1.

The seismometers used in this study were three-component STS-2 seismometers, located one each at the corner station and at the X and Y end stations. Along with these, two single-axis ground-rotation sensors (referred to as beam rotation sensor [BRS]) were installed at LHO, one at each end station, measuring rotation about the axis orthogonal to their respective arm axes. These are located ~1 m from the seismometers. Following the coordinate convention at LHO, we assign the X axis to be parallel to the X-arm, Y axis to be parallel to the Y-arm, and Z axis to be aligned with the gravitational vertical. Tilts measured along the Y axis (or about the X axis) are referred to as Y-tilt or angle.

The BRS used in this study consists of a 1-m-long beam balance suspended from 15-μm-thick flexures with a fundamental resonance frequency of 7.7 mHz. The angle of the beam relative to the ground is measured with a high-sensitivity autocollimator whose noise floor is ~0.2 nrad/$\sqrt{\text{Hz}}$ above 60 mHz. For more details on BRS, see Venkateswara *et al.* (2014). As the ground tilts at frequencies above the resonance of the beam balance, the beam stays inertial, hence the autocollimator measures the ground tilt.

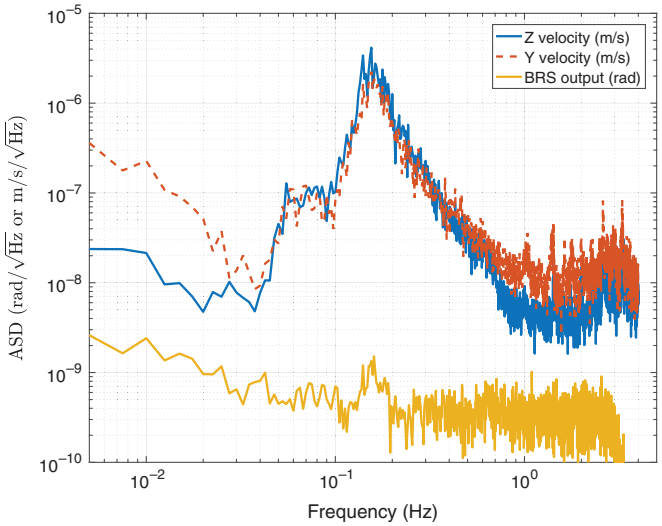

▲ **Figure 2.** Amplitude spectral density (ASD) of the signals during a 2000 s stretch before the arrival of the signals from the **M** 7.9 earthquake on 17 December 2016. The color version of this figure is available only in the electronic edition.

Translational acceleration coupling of a BRS is minimized by adjusting the center of mass to be close to the pivot point of the flexures. At frequencies greater than the resonance frequency of the beam balance, the strength of this coupling can be approximated with $M\delta/I$, in which M is the mass of the balance, I is the moment of inertia, and δ is the distance from the center of mass to the pivot point (Venkateswara *et al.*, 2014). For the BRS at EndX, δ was found to be 30 μm, after installation. Schedule constraints did not permit further adjustments. This δ leads to a translation coupling of 2×10^{-4} rad/m, which pollutes the tilt signal with translation at the frequencies of interest for teleseismic events. For the BRS at EndY, δ was tuned to less than 0.5 μm during installation. The very small value of δ for this instrument leads to a translation coupling of less than 1×10^{-6} rad/m and allows for precise measurement of the tilt component of low-frequency seismic waves.

Figure 2 shows the amplitude spectral density of the BRS signal along with two axes of the collocated seismometer before arrival of the Papua New Guinea earthquake on 17 December 2016, recorded at 10:30:00 UTC for 2000 s. Windspeeds were below 3 m/s during this period and therefore the BRS curve is representative of the noise floor of the instrument, which can resolve tilt amplitudes as small as 0.1 nrad for periods in the 10–50 s range.

In this study, we present phase-velocity estimations derived from tilt component measurements with the BRS at EndY of multiple teleseismic waves with a variety of angles of incidence and distances of origin from the facility. We did not analyze the data from the BRS at EndX due to its large horizontal motion coupling. In principle, if the value of δ was known precisely enough, this coupling could be removed from the data using the horizontal seismometer channel. The current uncertainty on δ introduces large errors in the rotation measurement

with BRS-X, thus it is not used in this study. For the remainder of this article the term BRS refers to only the BRS at EndY.

THEORETICAL FRAMEWORK

The plane-wave solution of a Rayleigh wave has three translational and three rotational components denoted by $(u_x, u_y, u_z, \theta_x, \theta_y, \theta_z)$, respectively, where subscripts denote the axes translations are along and rotations are about. They can be described by

$$u_x(\mathbf{r}, t) = \alpha \sin(\zeta) \cos(\psi) \cos(\omega t - \mathbf{k} \cdot \mathbf{r} + \phi), \tag{1}$$

$$u_y(\mathbf{r}, t) = \alpha \sin(\zeta) \sin(\psi) \cos(\omega t - \mathbf{k} \cdot \mathbf{r} + \phi), \tag{2}$$

$$u_z(\mathbf{r}, t) = \alpha \cos(\zeta) \cos(\omega t - \mathbf{k} \cdot \mathbf{r} + \pi/2 + \phi), \tag{3}$$

$$\theta_x(\mathbf{r}, t) = \frac{\partial u_z}{\partial y} = \alpha\kappa \cos(\zeta) \sin(\psi) \cos(\omega t - \mathbf{k} \cdot \mathbf{r} + \phi), \tag{4}$$

$$\theta_y(\mathbf{r}, t) = -\frac{\partial u_z}{\partial x} = -\alpha\kappa \cos(\zeta) \cos(\psi) \cos(\omega t - \mathbf{k} \cdot \mathbf{r} + \phi), \tag{5}$$

$$\theta_z(\mathbf{r}, t) = \frac{1}{2}\left(\frac{\partial u_y}{\partial x} - \frac{\partial u_x}{\partial y}\right) = 0, \tag{6}$$

in which α is the amplitude of the wave, ζ is the ellipticity angle, ψ is the angle of propagation, ω is the angular frequency of the wave, κ is the wavenumber, ϕ is the phase of the wave, $\mathbf{r}$ is the position vector, and $\mathbf{k}$ is the wave vector $\kappa(\cos(\psi), \sin(\psi), 0)$ (Maranó and Fäh, 2014). With the assumption that the wavenumber is constant over the region of interest, this gives us six parameters to fully describe the surface field of a Rayleigh wave. Measuring three axes of translation at a single point alone cannot fully characterize the wave, whereas measuring the three translations and two tilts is sufficient. Measurement of the θ_z is useful to distinguish between Love waves and Rayleigh waves but is more difficult because Love waves typically have even smaller amplitudes.

If the relevant components of a Rayleigh wave can be measured and the plane-wave assumption holds, then the phase velocity of the wave can be computed by

$$v = -\frac{\dot{u}_z}{\theta_x} \sin(\psi), \tag{7}$$

in which v is the wave phase velocity, $\dot{u}_z$ is the magnitude of the vertical seismometer velocity, θ_x is the tilt about the x axis, and ψ is the direction of propagation with respect to the x axis.

The phase velocity and angle can also be computed from the phase difference between a network of three seismometers located in an L-shape, as shown in Figure 1, by

$$v = \frac{d}{\sqrt{\Delta t_x^2 + \Delta t_y^2}} \tag{8}$$

$$\psi = \arctan\left(\frac{\Delta t_y}{\Delta t_x}\right), \tag{9}$$

in which d is the distance between the corner seismometer and the end seismometers, Δt_x and Δt_y are the delays of the time of arrival between the seismometers in the x and y directions, respectively.

EARTHQUAKE SIGNALS

A selection of recent earthquakes were chosen for this study, which showed prominent teleseismic tilt signals. Earthquake magnitude, distance from measurement site, activity (both environmental and anthropogenic) at the site, and angle of incidence can all influence whether or not the signal is prominent. Because of the geometry of the array and rotation sensor, our measurements were insensitive to waves traveling along EndX (northwest–southwest). Additionally, our instruments are sensitive to tilts driven by wind and human activity, which eliminated many candidate events in our search.

Figure 3a shows the time trace of the STS-2 seismometer and the BRS at the EndY from the 17 December 2016 magnitude 7.9 earthquake east of New Ireland, Papua New Guinea. The signals are band-passed between 10 and 300 mHz by a fourth-order Butterworth filter to focus on the earthquake signal. The first plot is the seismometer velocity along the Z direction, and the second plot is the angle about the X direction measured by BRS. The signals look nearly identical, as one expects from equations (3) and (4) if Rayleigh waves dominate the signal. The third plot shows the displacement measured along the Y direction. The Y displacement is qualitatively different from the signal in the BRS. Around $t = 1200$ s, a large amplitude signal is visible in the Y displacement, with much smaller corresponding signals in X angle or Z velocity, suggesting a shear wave. The small signal in BRS shows a displacement cross coupling of better than $\sim 3 \times 10^{-6}$ rad/m which translates to less than 3% error introduced from translation coupling. Figure 3b,c shows spectrograms of the two instruments starting at 1300 s before the earthquake origin time of 10:51:12 UTC.

In addition to the Papua New Guinea earthquake, we observed five other quality events shown in Figures 4–8. The collections of all six are those used in the phase-velocity analysis described below. The angles of incidence listed in Table 1 were estimated using equation (9) with the time delays measured by the seismometer array. All six events show similar time evolution in the Z velocity and X tilt.

PHASE-VELOCITY ANALYSIS

Temporal Analysis

One application of these measurements is the estimation of low-frequency Rayleigh-wave phase velocities. Phase-velocity

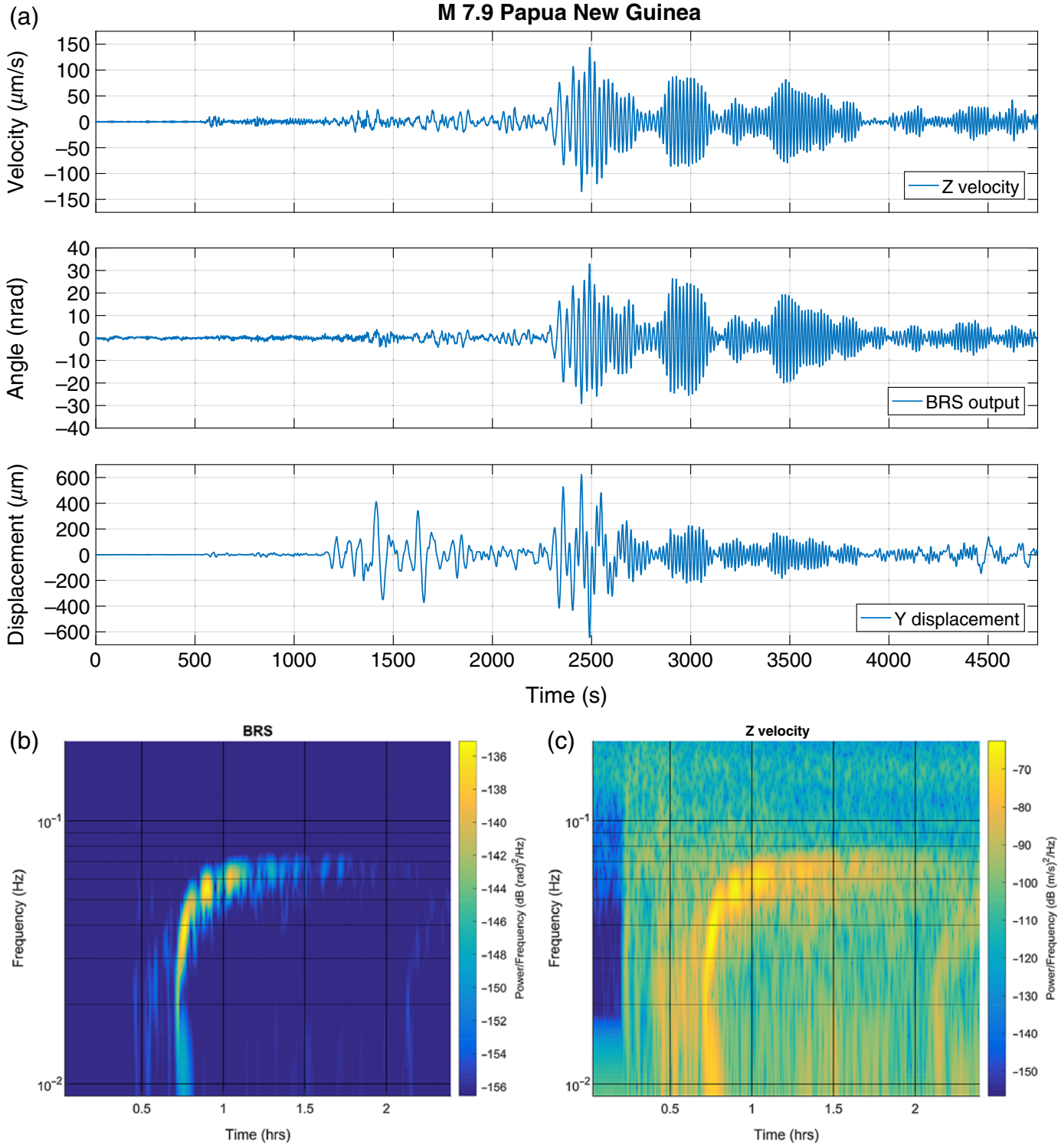

▲ **Figure 3.** (a) Time series of the 17 December 2016 magnitude 7.9 earthquake east of New Ireland, Papua New Guinea, band-pass filtered between 10 and 300 mHz. The *x* axis starts at the earthquake origin time of 10:51:12 UTC. Spectrogram of (b) tilt and (c) vertical velocity of the same event with the *x* axis extending 1300 s before the earthquake origin time and 2700 s after the end of (a). The color version of this figure is available only in the electronic edition.

measurements have direct applications in seismic-wave inversion problems (Haskell, 1953) and are traditionally done with large arrays of translational seismometers (Lin *et al.*, 2008).

Rayleigh-wave phase velocities can be obtained with the measured signals by exploiting equations (7) and (8). With the assumption that the incoming wave can be approximated

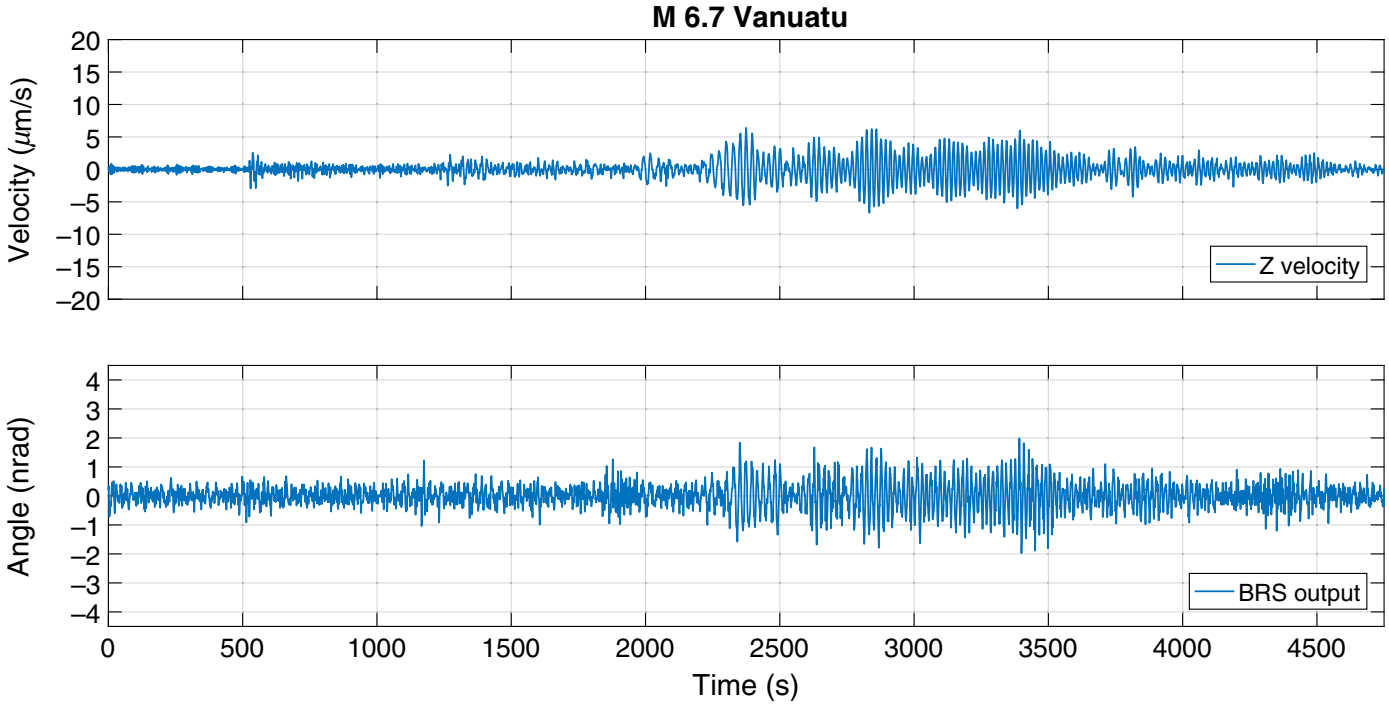

▲ **Figure 4.** Time series of the 6 April 2016 magnitude 6.7 earthquake 102 km west-southwest of Sola, Vanuatu, band-pass filtered from 30 to 300 mHz. The *x* axis starts at the earthquake origin time of 6:58:48 UTC. The color version of this figure is available only in the electronic edition.

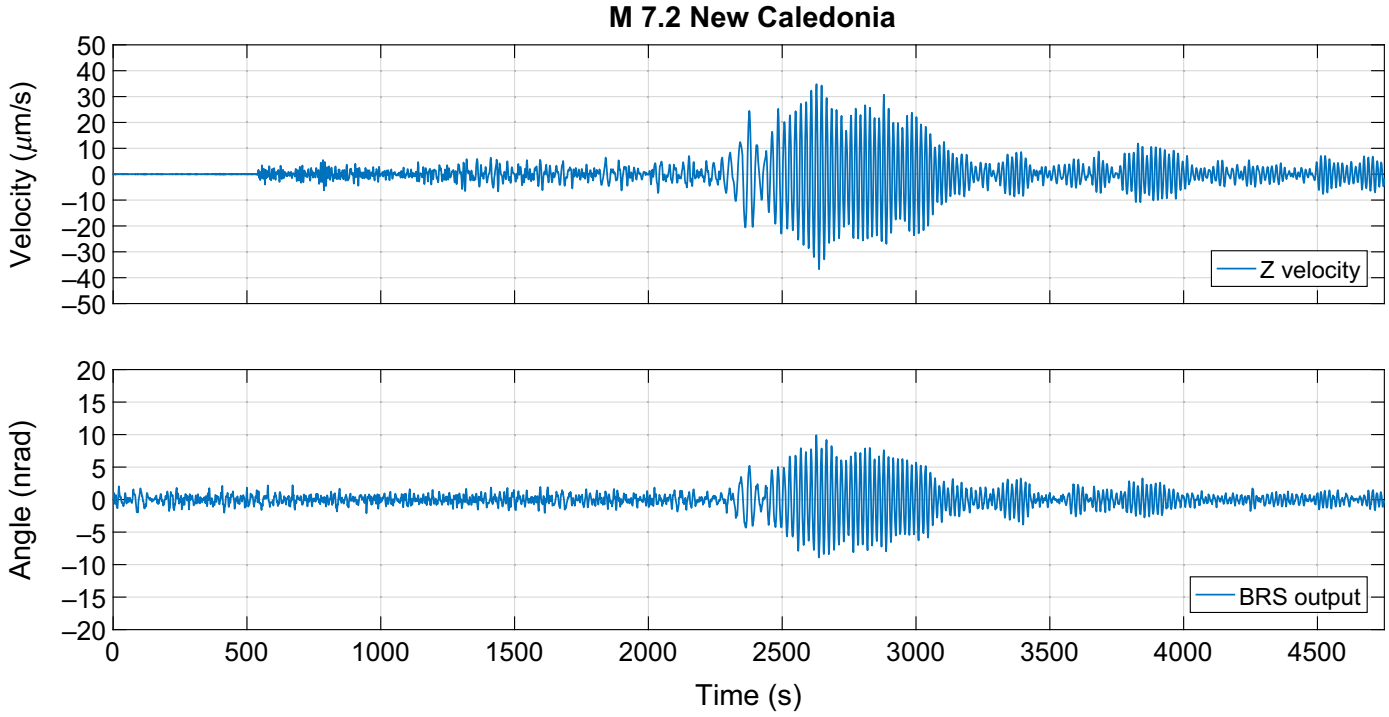

▲ **Figure 5.** Time series of the 12 August 2016 magnitude 7.2 earthquake 110 km east of Ile Hunter, New Caledonia, band-pass filtered from 30 to 300 mHz. The *x* axis starts at the earthquake origin time of 01:26:36 UTC. The color version of this figure is available only in the electronic edition.

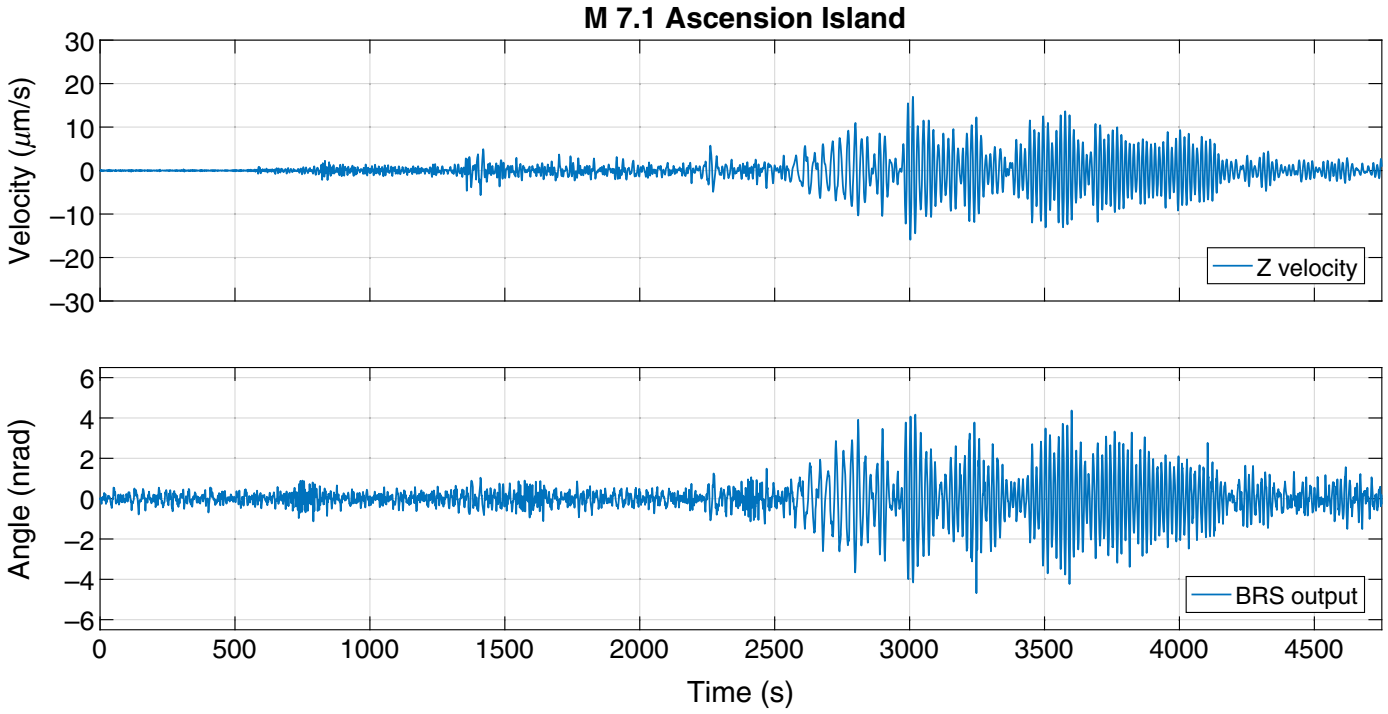

▲ **Figure 6.** Time series of the 29 August 2016 magnitude 7.1 earthquake north of Ascension Island, band-pass filtered from 30 to 300 mHz. The *x* axis starts at the earthquake origin time of 04:29:57 UTC. The color version of this figure is available only in the electronic edition.

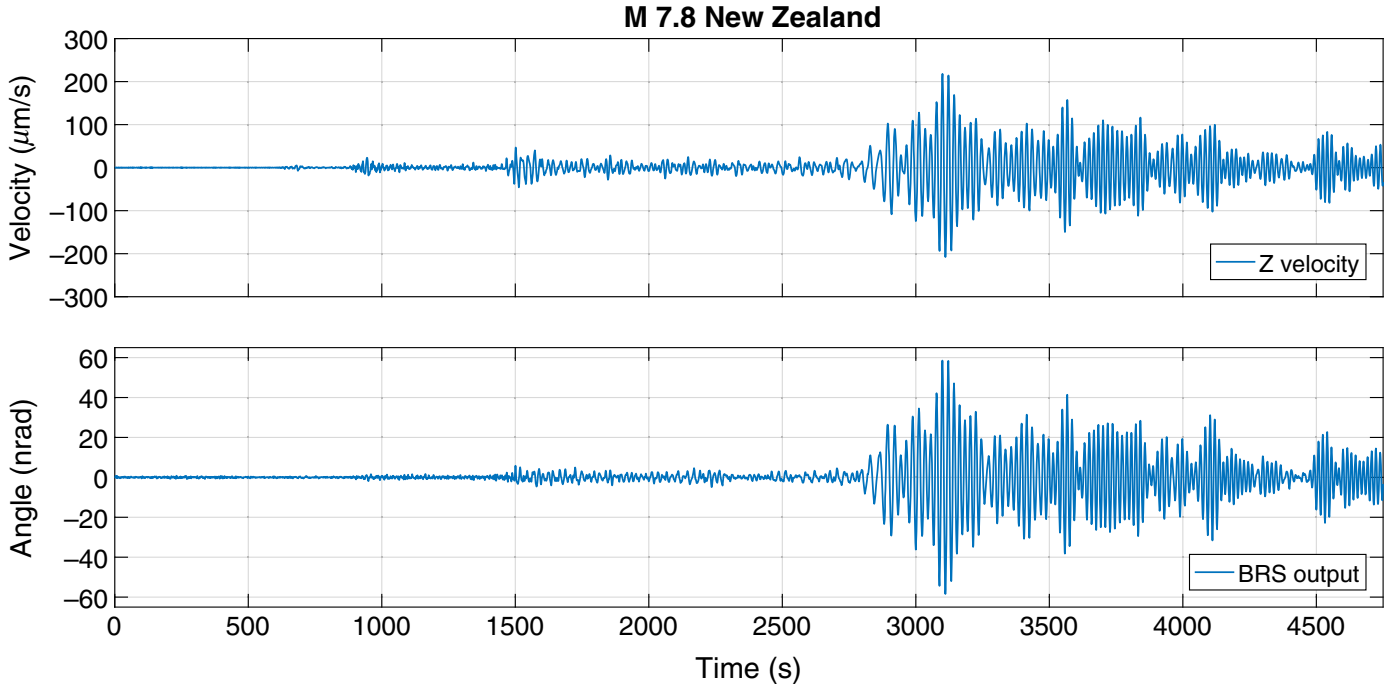

▲ **Figure 7.** Time series of the 13 November 2016 magnitude 7.8 earthquake 54 km north-northeast of Amberley, New Zealand, band-pass filtered from 30 to 300 mHz. The *x* axis starts at the earthquake origin time of 11:02:56 UTC. The color version of this figure is available only in the electronic edition.

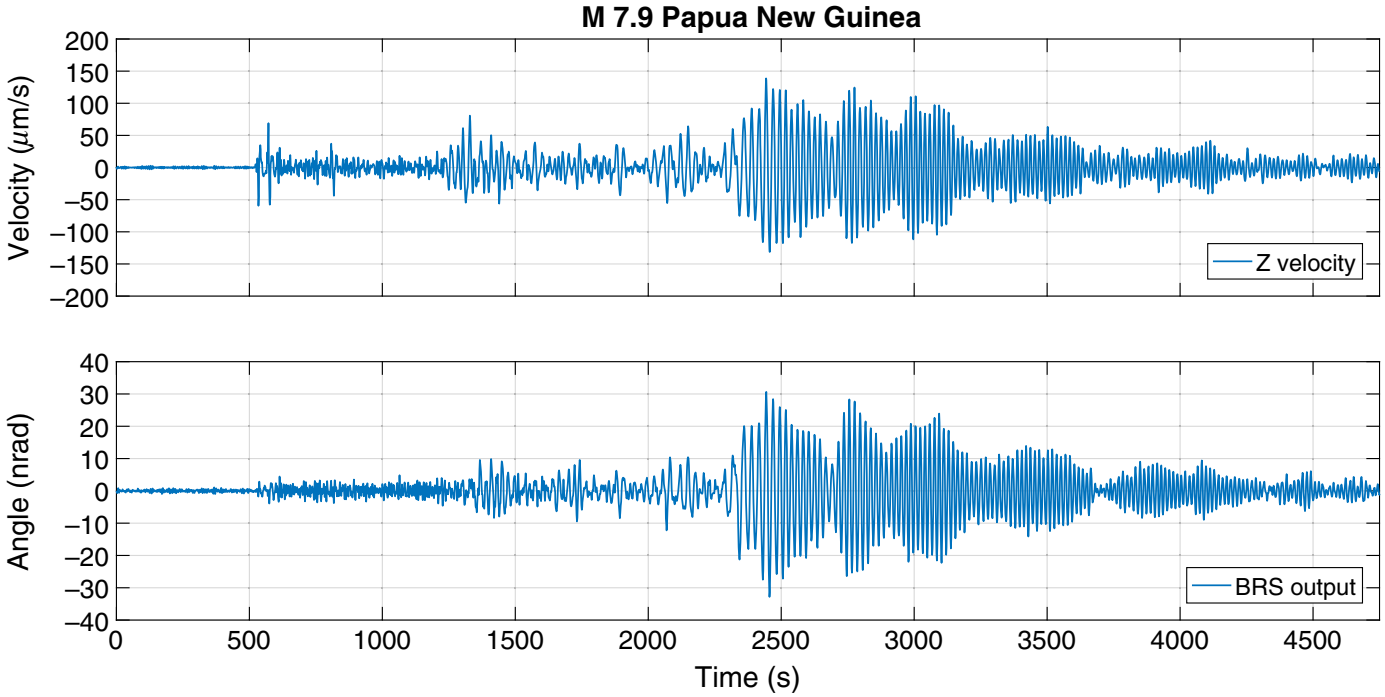

▲ **Figure 8.** Time series of the 22 January 2017 magnitude 7.9 earthquake 35 km west-northwest of Panguna, Papua New Guinea, band-pass filtered from 30 to 300 mHz. The *x* axis starts at the earthquake origin time of 04:30:22 UTC. The color version of this figure is available only in the electronic edition.

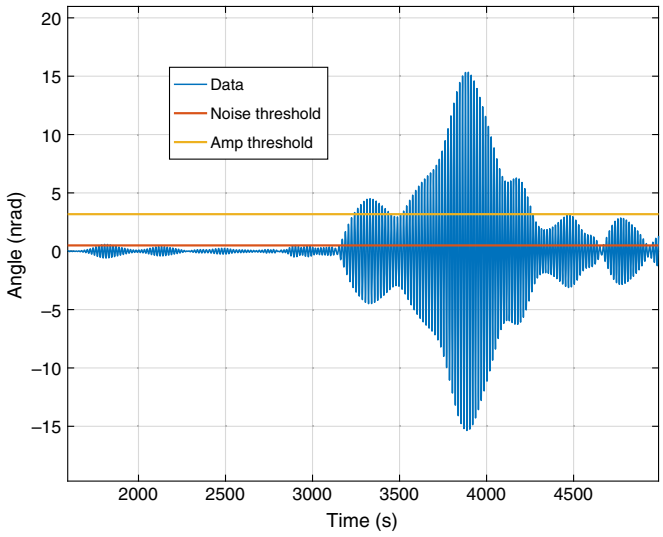

▲ **Figure 9.** Beam rotation sensor (BRS) data from the 17 December 2016 Papua New Guinea earthquake band-pass filtered at 60 mHz along with the noise threshold and amplitude threshold. The noise threshold is set to five times the BRS instrumental noise and is held constant for all frequencies and events. The amplitude threshold is set to 10% of the maximum value attained by the BRS before filtering. This changes from event to event but is the same for all frequencies which focuses the analysis on the loudest sections of data as they are likely the primary shortest-path surface waves. The color version of this figure is available only in the electronic edition.

by a single plane wave, one would expect consistent results from both equations. This allows us to provide useful local geophysical parameters while also demonstrating an application of teleseismic tilt measurements.

To extract phase dispersion curve estimates, each channel was separated into frequency bins by band-passing the time series with 5 mHz-wide third-order Butterworth filters that were centered at frequencies stepped through the band of interest (25–65 mHz) in 5 mHz steps.

Phase velocity and angle of incidence estimations were first done using the array of translational seismometers. By equations (8) and (9), one only needs the delays of time of arrival between the stations to reconstruct the phase velocity and angle because the distance is well known. These are computed by finding the center of a Gaussian that is fit to the central peak of the cross correlation of 10 period-long cuts of the corner station and the end-station signals for both the X and Y directions. The mean of the velocities and angles were then taken to yield a single value per frequency bin.

A second set of phase-velocity estimations were made using the amplitudes of the tilt signal from the BRS and the vertical component of the seismometer by equation (7). Although it is theoretically possible to obtain single-station measurements of the angle of incidence from the ratio of either the horizontal translation or rotation signals, Love-wave contamination and the lack of an orthogonal (θ_y) tilt measurement required our analysis to use the angle of incidence calculated from the seismometer array. The amplitudes were computed by fitting quarter-period long-time series to a sinusoidal function.

Table 1
Earthquakes Captured in This Analysis

Time of Event (yyyy/mm/dd hh:mm:ss)	Location of Epicenter	Magnitude	Measured Angle (°)	Calculated Angle (°)
2016/04/06 06:58:48	102 km west-southwest of Sola, Vanuatu	6.7	70.1 ± 2.7	75.4
2016/08/12 01:26:36	110 km east of Ile Hunter, New Caledonia	7.2	86.0 ± 2.0	85.5
2016/08/29 04:29:57	North of Ascension Island	7.1	−110.9 ± 0.8	−117.4
2016/11/13 11:02:56	54 km north-northeast of Amberley, New Zealand	7.8	89.7 ± 1.9	98.9
2016/12/17 10:51:12	46 km east of Taron, Papua New Guinea	7.9	67.0 ± 2.0	59.4
2017/01/22 04:30:22	35 km west-northwest of Panguna, Papua New Guinea	7.9	56.9 ± 1.0	61.8

Angles referenced counter clockwise from the *X* axis. Measured angles are estimated using equation (9) averaged over time bins as described in the Temporal Analysis section with errors representing one standard deviation. Calculated angles are from great circle calculations. Times (UTC), magnitude, and location are courtesy of U.S. Geological Survey.

The resultant velocities were then averaged together for each frequency bin.

Two amplitude thresholds were applied to remove sections of data that were noise dominated and those that did not contain the primary surface wave, one at five times the BRS sensor noise and one at 10% of the maximum amplitude of the BRS signal before filtering. These are shown in Figure 9 along with a typical filtered time series. An additional cut that required the phase difference between the BRS and seismometer signals to be no more than 20° was implemented to restrict our analysis to only Rayleigh waves, as other wave types would not typically be in-phase with the tilt signal. Because of the nature of these earthquakes, our thresholds restrict each earthquake to the band for which it has prominent tilt signal. The resultant dispersion curves are shown in Figure 10a, which show agreement with the array measurements across the band for the three highest magnitude events. However, we observe some disagreement at lower frequencies for the lower SNR, **M** 7.2 and 7.1 events, which is likely due to noise contaminations of the tilt amplitude measurements.

Spectral Analysis

We performed a separate, more traditional, analysis which calculated phase differences and relative amplitudes from the spectral transfer function of relevant signals (Meier *et al.*, 2004; Legendre *et al.*, 2015). Equations (8) and (9) were then used to find the corresponding phase velocities for the array and single-station methods. The mean phase velocity in 5-mHz-wide bins were then taken to be the phase velocity for each frequency shown in Figure 10b. Bins that yielded delays with standard deviation larger than 0.2 s were discarded as these corresponded to bins that were noise dominated.

Although the spectral method avoids systematic errors produced by narrow filtering, it cannot distinguish between primary Rayleigh waves and other types of seismic activity. This led us to develop the temporal method which, along with wave-type discrimination, can measure phase-velocity evolution in time.

CONCLUSION

We presented high-SNR measurements of the tilt component of surface waves from multiple teleseismic events with a ground-rotation sensor installed at LHO and have shown that a collection of these measurements can yield consistent Rayleigh-wave phase-velocity measurements when compared with an array of seismometers. These measurements demonstrate the ability to resolve local seismological parameters using seismometers and rotation sensors at a single station and are enabled by the high tilt sensitivity and low translational-motion coupling of the beam rotation sensor making it a useful tool in rotational seismology.

A more sophisticated analysis which takes into account the anisotropy of the earth, the multimode and multiwave nature of the events, and other complex phenomena are likely to reveal further geophysical information with these datasets. Both beam rotation sensors installed at LHO are permanent pieces of the observatory's seismic isolation and will continue operation for the foreseeable future.

DATA AND RESOURCES

The data and analysis used in this article can be found at https://dcc.ligo.org/LIGO-P1700149/public (last accessed August 2017).

ACKNOWLEDGMENTS

This work was carried out at the Laser Interferometer Gravitational-Wave Observatory (LIGO) Hanford Observatory (LHO) by members of LIGO laboratory and the LIGO Scientific Collaboration including University of Washington, Seattle, and Harvard University. LIGO was constructed by the California Institute of Technology and Massachusetts Institute of Technology with funding from the National Science Foundation (NSF) and operates under Cooperative Agreement PHY-0757058. Advanced LIGO was built under Award PHY-0823459. This document has been assigned LIGO Lab-

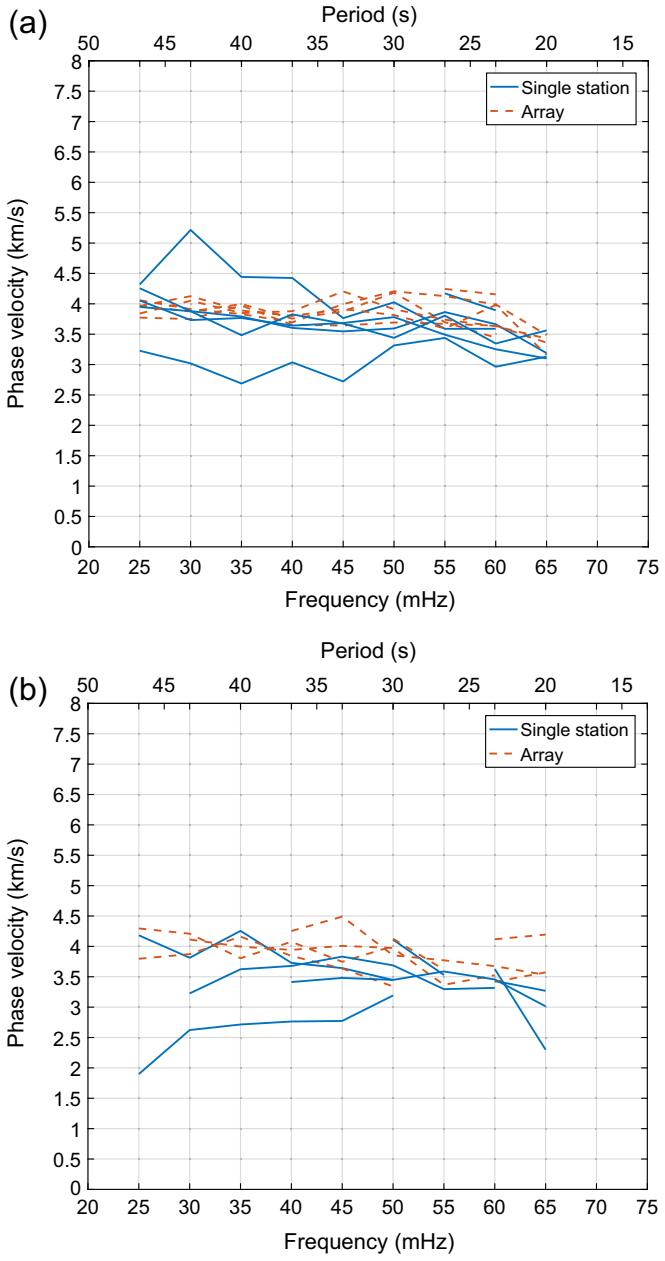

▲ **Figure 10.** Phase velocity for a collection of six teleseismic events calculated using (a) the temporal analysis and (b) the spectral analysis as described above. Single station indicates that velocities were calculated from the ratio of vertical motion and tilt motion, whereas array indicates velocities measured using the time delay between vertical seismometers. The color version of this figure is available only in the electronic edition.

oratory document number LIGO-P1700149. Participation from the University of Washington, Seattle, was supported by funding from the NSF under Awards PHY-1306613 and PHY-1607385.

The authors would like to thank the LHO staff for their assistance with the installation and maintenance of the sensors. The authors are also grateful for the useful comments and suggestions by Jan Harms and for the many thought-provoking discussions with our colleagues in the Eöt-Wash Group. Additionally, the authors thank the Center for Experimental Nuclear Physics and Astrophysics (CENPA) for use of its facilities and Brian Lantz for the useful MATLAB scripts.

REFERENCES

Aasi, J., B. P. Abbott, R. Abbott, T. Abbott, M. R. Abernathy, K. Ackley, C. Adams, T. Adams, P. Addesso, R. X. Adhikari, *et al.* (2015). Advanced LIGO, *Class. Quantum Grav.* **32,** no. 7, 074001.

Belfi, J., N. Beverini, G. Carelli, A. Di Virgilio, E. Maccioni, G. Saccorotti, F. Stefani, and A. Velikoseltsev (2012). Horizontal rotation signals detected by "g-pisa" ring laser for the $M_w = 9.0$, March 2011, Japan earthquake, *J. Seismol.* **16,** no. 4, 767–776.

Haskell, N. A. (1953). The dispersion of surface waves on multilayered media, *Bull. Seismol. Soc. Am.* **43,** no. 1, 17–34.

Lantz, B., R. Schofield, B. O'Reilly, D. E. Clark, and D. DeBra (2009). Review: Requirements for a ground rotation sensor to improve advanced LIGO, *Bull. Seismol. Soc. Am.* **99,** no. 2B, 980–989.

Lee, W. H. K., M. Celebi, M. I. Todorovska, and H. Igel (2009). Introduction to the special issue on rotational seismology and engineering applications, *Bull. Seismol. Soc. Am.* **99,** no. 2B, 945–957.

Legendre, C. P., L. Zhao, W.-G. Huang, and B.-S. Huang (2015). Anisotropic Rayleigh-wave phase velocities beneath northern Vietnam, *Earth Planets Space* **67,** no. 1, 28.

Lin, C.-J., H.-P. Huang, N. D. Pham, C.-C. Liu, W.-C. Chi, and W. H. K. Lee (2011). Rotational motions for teleseismic surface waves, *Geophys. Res. Lett.* **38,** no. 15, L15301, doi: 10.1029/2011GL047959.

Lin, F.-C., M. P. Moschetti, and M. H. Ritzwoller (2008). Surface wave tomography of the western United States from ambient seismic noise: Rayleigh and Love wave phase velocity maps, *Geophys. J. Int.* **173,** no. 1, 281–298.

Maranó, S., and D. Fäh (2014). Processing of translational and rotational motions of surface waves: Performance analysis and applications to single sensor and to array measurements, *Geophys. J. Int.* **196,** 317–339.

Matichard, F., B. Lantz, R. Mittleman, K. Mason, J. Kissel, B. Abbott, S. Biscans, J. McIver, R. Abbott, S. Abbott, *et al.* (2015). Seismic isolation of advanced LIGO: Review of strategy, instrumentation and performance, *Class. Quantum Grav.* **32,** no. 18, 185003.

Meier, T., K. Dietrich, B. Stöckhert, and H. Harjes (2004). One-dimensional models of shear wave velocity for the eastern Mediterranean obtained from the inversion of Rayleigh wave phase velocities and tectonic implications, *Geophys. J. Int.* **156,** no. 1, 45–58.

Pancha, A., T. H. Webb, G. E. Stedman, D. P. McLeod, and K. U. Schreiber (2000). Ring laser detection of rotations from teleseismic waves, *Geophys. Res. Lett.* **27,** no. 21, 3553–3556.

Reinwald, M., M. Bernauer, H. Igel, and S. Donner (2016). Improved finite-source inversion through joint measurements of rotational and translational ground motions: A numerical study, *Solid Earth* **7,** no. 5, 1467–1477.

Venkateswara, K., C. A. Hagedorn, J. H. Gundlach, J. Kissel, J. Warner, H. Radkins, T. Shaffer, B. Lantz, R. Mittleman, F. Matichard, *et al.* (2017). Subtracting tilt from a horizontal seismometer using a ground rotation sensor, *Bull. Seismol. Soc. Am.* **107,** no. 2, 709–717.

Venkateswara, K., C. A. Hagedorn, M. D. Turner, T. Arp, and J. H. Gundlach (2014). A high-precision mechanical absolute-rotation sensor, *Rev. Sci. Instrum.* **85,** no. 1, 015005.

M. P. Ross
K. Venkateswara
C. A. Hagedorn
J. H. Gundlach
Center for Experimental Nuclear Physics and Astrophysics

(CENPA)
University of Washington
4311 Mason Pl NE
Seattle, Washington 98105 U.S.A.
mpross2@uw.edu

J. S. Kissel
J. Warner
H. Radkins
T. J. Shaffer
LIGO Hanford Observatory
127124 N Rt. 10
Richland, Washington 99352-0159 U.S.A.

M. W. Coughlin
LIGO Laboratory
California Institute of Technology
MC 100-36
Pasadena, California 91125 U.S.A.

P. Bodin
Department of Earth and Space Sciences
University of Washington
4000 15th Avenue NE
Seattle, Washington 98195-1310 U.S.A.

Published Online 15 November 2017